City Research Online

City, University of London Institutional Repository

This is the published version of the paper.

This version of the publication may differ from the final published version.

Refractive index and temperature dual-parameter sensors based on loss mode resonance and directional coupler in side-polished hole-assisted dual-core fiber

YUAN JIN,[1] LAI GAO,[1] YUXIAO XUE,[1] JING YANG,[1,3] YAN LIU,[1] ZHENG ZHU,[1] JINHUI SHI,[1] K. T. V. GRATTAN,[2] AND CHUNYING GUAN[1,4]

[1]*Key Laboratory of In-Fiber Integrated Optics of Ministry of Education, College of Physics and Optoelectronic Engineering, Harbin Engineering University, Harbin 150001, China*
[2]*School of Mathematics, Computer Science and Engineering, City, University of London, Northampton Square, London, EC1V 0HB, United Kingdom*
[3]*yangjing13@hrbeu.edu.cn*
[4]*cyguan@163.com*

Abstract: A refractive index (RI) and temperature dual-parameter sensor, based on a side-polished hole-assisted dual-core fiber (HADCF), has been proposed. In this sensor, SnO_2 film has been deposited on the suspended core of HADCF by RF sputtering to produce loss mode resonance (LMR). The energy of the center core has been shown to be able to be coupled into the suspended core, taking advantage of the small distance involved and phase matching between two cores. The 10 mm long HADCF can be used to form a directional coupler. LMR and the directional coupler are integrated in parallel on the same section of HADCF, which realizes the high integration of sensing measurement. The sensor achieves simultaneous measurement of both RI and temperature through measuring both the LMR dip and coupling dip. The RI and temperature sensitivities achieved were 3812.5 nm/RIU and 521.4 pm/°C, respectively. The sensor discussed shows important advantages of high sensitivity, simple fabrication, high integration, and the ability to make measurements of two key parameters.

1. Introduction

Optical fibers have the advantages of allowing long-distance signal transmission, are of small size, available at low cost and show immunity to electromagnetic interference. Optical fiber sensors which are combined with nanomaterials have been widely used in several fields, such as biological science, medicine, and in chemistry. In recent years, sensors of this type based on thin film deposition have attracted significant attention, especially those using surface plasmon resonance (SPR) [1] and loss mode resonance (LMRs) [2] effects. Such sensors, based on SPR, have high sensitivity [3]. For example, a SPR sensor based on a micro-structured optical fiber coated by a MoS_2 film can create a high refractive index (RI) sensitivity, of 14600 nm/RIU [4]. SPR occurs when the real part of the dielectric constant of the film is negative and is higher than the imaginary part and the dielectric constant of the material around the film. When the real part of the thin-film permittivity is positive and higher in magnitude than its own imaginary part and also higher than real part of the permittivity of both the optical waveguide and the external medium surrounding the thin film, the resonance generated is termed loss mode resonance (LMR). In contrast, LMR can be obtained from a wider range of materials, such as polymers and metal oxides (SnO_2 [5], Al_2O_3 [6], ITO [7], TiO_2 [8], ZnO [9], etc.). Additionally, SPR only responds to transverse magnetic (TM) polarized light and is sensitive to the polarization of the incident light, whereas LMR can be excited under both transverse electric (TE) and TM polarizations.

Therefore, the LMR effect has been applied in both physical and biological sensing, in that way supporting the development of a range of optical fiber sensing devices [10–13].

In 2010, optical fiber sensor based on LMR was first experimentally demonstrated. This sensor utilized an unclad fiber dip coating of ITO, and had a refractive index (RI) sensitivity of 1617.4 nm/RIU [14]. In 2019, Wang et al. reported a fiber LMR sensor coated by SnO_2 thin film, and further, SnO_2 nanoparticles were used to improve the RI sensitivity [15]. To achieve a high sensitivity from such LMR sensors, single-mode fibers (SMFs) or multimode optical fibers (MMFs) are generally polished or etched to create D-type or tapered optical fibers [16–17], to enhance the evanescent field, and then a sensitizing thin film is coated on the appropriate region. For instance, the RI sensitivity of a D-type fiber coating with SnO_2 nanofilm is 14510 nm/RIU near the RI of 1.321, close to the RI of water, a feature which is crucial in biosensor applications [18]. Ozcariz et al. have presented LMR sensors based on InGa-Zn-Oxide (IGZO) thin-films, employing two types of optical fiber: MMF with an exposed core and D-shaped SMF [19]. The impact of the polishing depth on the LMR characteristics of the D-shaped fiber has also been investigated. The LMR optical fiber sensor, fabricated by depositing a thin metal oxide film on a uniform fiber taper waist region sandwiched between two unclad tapered fibers, has been numerically analyzed. Compared with the traditional fiber probe based on SPR, the LMR sensor developed has demonstrated an approximately threefold improvement in sensitivity [20].

The multi-parameter sensing capability illustrated has been very useful, as the testing environment is complex. There are many methods to measure RI and temperature simultaneously, such as using tapered fibers [21], Long-period fiber gratings (LPFGs) [22], fiber Bragg gratings (FBGs) [23] and interferometers [24]. In this paper, a RI and temperature dual-parameter sensor were demonstrated based on a side-polished hole-assisted dual-core fiber (HADCF). SnO_2 film sputtered onto the suspended core of side-polished HADCF excites the LMR. Meanwhile, the mode coupling occurs due to the small distance and phase matching between the cores [25]. The size of the sensor can be reduced by integrating LMR and directional coupler in parallel on the same HADCF section. The sensor illustrated achieves simultaneous measurement of both RI and temperature by monitoring the LMR dip and coupling dip. The RI and temperature sensitivities achieved were 3812.5 nm/RIU and 521.4 pm/°C, respectively. In addition, it has advantages such as simplicity in manufacture, a high level of integration, and the potential for measurement of more biochemical parameters.

2. Structure and principle of optical fiber sensor

Loss mode resonance (LMR) is a coupling phenomenon between the transmission waveguide mode and the loss mode of a thin film, at a specific thickness. Excitation of LMR requires two conditions: coincidence of mode field between two modes and meeting of phase matching condition. At the phase matching wavelength, the guided mode in the waveguide couples to the loss mode in the thin film, so that the transmission is obviously attenuated [26]. Consequently, one or more LMR dips are obtained in the transmission spectrum. The nano-film coated region serves as the sensing area of the device. As the RI of the surrounding environment fluctuates, the effective RI of the loss mode in the film also varies, leading to a change in the resonant wavelength.

The HADCF was drawn by our laboratory and is composed of a center core, an air hole, an eccentric core suspended on the inner wall of the air hole, and the cladding, as shown in Fig. 1(a). The diameters of the cladding, air hole, center core and suspended core are 125 μm, 45 μm, 9.5 μm, and 11 μm, respectively. The distance between the centers of the two cores was 15.5μm. The RIs of two cores are the same and the RI difference between the core and the cladding is 0.005. A schematic diagram of the proposed LMR sensor is presented in Fig. 1(d). The 10 mm-long HADCF has been precisely welded between two pieces of SMF, by using a commercial welding machine (FSM-100P+). When the offset distance between the end faces of

the two optical fibers is 15.5 μm, the loss in the transmission spectrum is minimum and there is no additional interference in the spectrum, indicating that almost all the energy from the SMF has been transmitted into the suspended core of HADCF. Subsequently, the HADCF was polished using a side-polishing instrument (constructed in our laboratory). The orientation of the HADCF was adjusted by viewing through the optical microscope, so that the air hole side was facing directly up. The polishing length was 10 mm and polishing depth, 20 μm. The suspended core of the polished HADCF was exposed to the air as shown in Fig. 1(b). The polished sample was placed in an ultrasonic cleaner to remove the remaining fiber debris from its surface. The SnO_2 used has a high real part of the RI and low extinction coefficient in long wavelength, and it is an ideal material for exciting LMR. Using the magnetron sputtering system available (JGP-450B, SKY Technology Development Co., Ltd. Chinese Academy of Science), SnO_2 film was deposited on the surface of the suspended core by RF sputtering, where the SnO_2 target with a purity of 99.99%. The sputtering process was done under a pressure of 5×10^{-1} Pa and a voltage of 30 V, so that the sputtering rate of SnO_2 was 1 nm/s. Figure 1(c) shows the SEM image of the SnO_2 film deposition region. The SnO_2 thin film was composed of crystal particles, where the crystal particle size was uniform, the crystallinity was good, and the film surface roughness was small. It can be seen that the thickness of SnO_2 film was non-uniform and non-concentric with the suspended core, due to the curve surface of the core. In addition, the angle, position and distance of the fiber relative to the target also are known to affect the uniformity of the film.
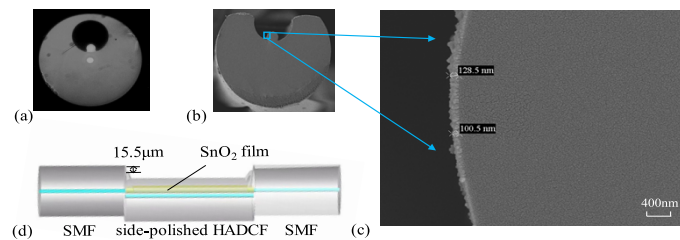
Fig. 1. The HATCF and sensor structure. (a) Image of the HATCF obtained using a microscope. (b) SEM image of the side-polished HATCF. (c) High magnification image of the SnO_2 film deposition region in Fig. 1(b). (d) Schematic diagram of the sensor design.

The effects of the SnO_2 film thickness on the LMR wavelength were analyzed by using the finite element method (FEM). The RI of the SnO_2 was 1.9522 at 1550 nm. In simulations, the dispersion of SnO_2 was considered by using the Lorentz oscillator model. The confinement loss (*CL*) was calculated through knowing the imaginary part of mode effective RI (n_{eff}) and based on the following relationship [27].

$$CL(\text{dB/cm}) = \frac{2\pi \times 8.686 \times 10000 \times \text{Im}(n_{eff})}{\lambda} \tag{1}$$

where, λ is the wavelength of the light used. Figure 2 shows the model of the suspended core used in the simulation, with a 90 nm SnO_2 film. Firstly, the uniform SnO_2 film with thickness of 90 nm was covered on the suspended core of the HADCF, and then the whole SnO_2 film was shifted to the right by 90 nm, as a result of which the SnO_2 film was non-concentric with suspended core and is similar in shape to a crescent. In this case the thickness of the SnO_2 film was defined to be 90 nm.

Figure 3(a) shows the effect of the SnO_2 film thickness on the transmission spectrum in a liquid (with RI = 1.333), where the film thickness ranged from 90 to 100 nm with a 5 nm interval. The actual thickness of the SnO_2 film is required as the resonance peak exhibits a red shift, as the thickness of the SnO_2 film increases. The transmission spectrum has three peaks in the wavelength range, 1100 to 1700nm, which correspond to the coupling between the 6th-,

4th-, 2nd-order loss modes and the fundamental mode, respectively. The longer the resonant wavelength, the lower the LMR mode order. Figure 3(b) illustrates the dispersion curves of the fundamental mode (blue line) of the suspended core and the higher-order modes (red, yellow and green lines) in the SnO_2 film, with the thickness set to be 100 nm. The insets are the electric field distributions of 6th-, 4th-, 2nd-order modes in the SnO_2 film and the fundamental mode in the suspended core. The LMR occurs in the wavelength region where the two dispersion curves are close to each other. The closest wavelengths between the dispersion curves of the fundamental mode of the suspended core and 6th-, 4th-, 2nd-order modes in the SnO_2 film were at 1264 nm, 1413 nm and 1685 nm, respectively. Only the even-order modes in the SnO_2 film were excited due to the 2-fold symmetry of the suspension core and film. The effective RIs of the 6th- and 4th-order modes lie closer to that of the fundamental mode, so these two resonance peaks are narrower and more sharp. However, the effective RI difference between the fundamental mode and the 2nd-order mode was relatively large and the coupling between two modes was weak, so the 2nd-order LMR peak was broad and flat. The SnO_2 film thickness in the range of 90 - 100 nm showed little effect on the loss magnitude of the resonance peak. The deviation between the results of the simulation and the experiment could be attributed to the fact that the actual coating shape and thickness of SnO_2 film cannot be exactly the same as the simulation. The SnO_2 film thickness was selected to be 100 nm in the experiment.
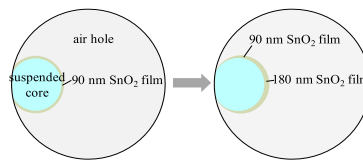
Fig. 2. Model of suspended core with SnO_2 film of 90 nm thickness used in the simulation.
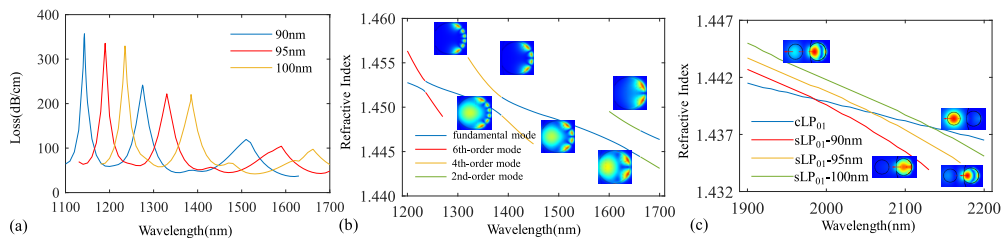
Fig. 3. (a) Confinement loss spectra of the suspended core with different thicknesses of the SnO_2 film. (b) Dispersion curves of the fundamental mode (blue line) in the suspended core and the higher-order modes (red, yellow and green lines) in the film with thickness of 100 nm. The inserts are the electric field distributions of fundamental mode, 6th-, 4th-, and 2nd-order loss modes. (c) Dispersion curves of the cLP_{01} and the sLP_{01} modes for different thicknesses of SnO_2 film. The inserts show the electric field distributions of the cLP_{01} and the sLP_{01} modes.

Due to the short distance used, the coupling between two cores will occur when the effective RIs of the fundamental modes in the center and suspended cores are equal or very close. Near the phase matching wavelength, the two cores can exchange energy with each other and a directional coupler is formed, where the energy ratio in the two cores at the output end of HADCF depends on the fiber length. The energy of the suspended core could be completely coupled into the center core, when the length of the HADCF is an odd multiple of the coupling length [25]. Figure 3(c) shows the dispersion curves between the fundamental mode in the center core (cLP_{01}) and the fundamental mode in the suspended core (sLP_{01}), in the wavelength range 1900-2100

nm, for different thicknesses of SnO_2 film. The insets show the electric field distributions of the fundamental modes in these two cores. The effective RI of cLP_{01} mode was unchanged and the effective RI of sLP_{01} mode increases with the increase of the SnO_2 film thickness. When the thickness of SnO_2 film was 90, 95 and 100 nm, the coupling peaks were seen at wavelengths of 1984, 2056 and 2130 nm, respectively. In the experiment, a 10 mm HADCF had been selected to form the coupler.

The resonant peaks of LMR and coupler each will exhibit distinct responses to RI and temperature, due to the different mechanisms, a feature which makes the sensor able to realize dual-parameter sensing.

3.   Experimental results and discussions

A supercontinuum laser (Superk Compact, NKT Photonics Company) has been used as the light source, and an Optical Spectrum Analyzer (OSA, AQ6370D) was employed to detect the transmission spectra. The experimental system is as shown in Fig. 4. The sample prepared was affixed to a glass slide, and then inserted vertically into a beaker with salt solution. The spiral micrometer pushed the connecting rod down into the solution to allow precise adjustment of the depth, L, of the immersion in the solution. The displacement of the spiral micrometer rod used was the same as that of the sample in the liquid.
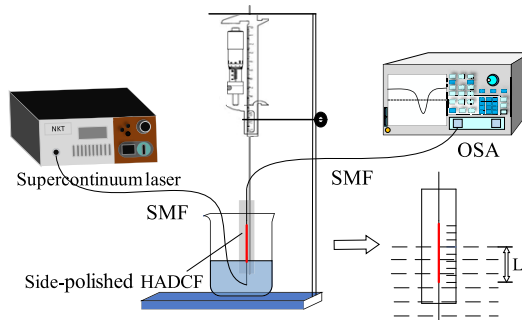

Fig. 4. Schematic diagram of test system used for RI sensing.

In the experiment carried out, the LMR and the directional coupler were used to realize the dual parameter sensing of the RI and temperature, respectively. The transmission spectra of samples coated with different SnO_2 film thicknesses for $L = 6$ mm are presented in Fig. 5(a), over the wavelength range 1000-1500 nm. For a film thickness of 90 nm, the insertion loss was seen to be ~13 dB, and the resonant dips that occur at 1055 nm and 1253 nm can be attributed to the coupling between 6th- and 4th-order LMR modes and fundamental mode, respectively. For a film thickness of 100 nm, two resonance dips were seen at 1145 nm and 1382 nm, and the depths of the dips were -23.6 dB and -22.7 dB, respectively. As the sputtering coating time increased, the thickness of the SnO_2 thin film increased, causing the LMR dips to shift towards longer wavelengths. The transmission spectrum of the sample coated with a 100 nm thickness SnO_2 film, observed in the range of 1200-2100 nm, is shown in Fig. 5(b). Dip 1 (1382 nm) and Dip 3 (1764nm) can be attributed to 4th- and 2nd- LMR, respectively. The weak coupling between the 2nd- LMR mode and the fundamental mode of the suspended core generates a minor dip (Dip 3) and the loss was less than 5 dB. Dip 2 (seen at 1935nm) can be attributed to the coupling between the suspended core and the center core of the HADCF. The experimental results obtained were in good agreement with the results of the simulation carried out. Figure 6 illustrates the transmission spectra of a sample coated with a 100 nm SnO_2 film, for different depths of immersion into water. When the immersion depth was less than 5 mm, the LMR

could not be excited. A better shape for the dip is observed at 6 mm immersion depth, where the bandwidth of LMR is significantly widened, when L exceeded 6 mm. The non-uniform thickness of the film results in the wide LMR dip seen, which can be understood as the overlap of several resonances generated by the different thickness films [5]. The coupler goes through under-coupling, coupling and over-coupling during the immersion of the sample in the water. When L has a value of 6-7 mm, the shape of the coupling dip is seen to improve. As a result, in the experiments which subsequently were undertaken, samples were immersed in the test solution to a depth of ~6 mm.
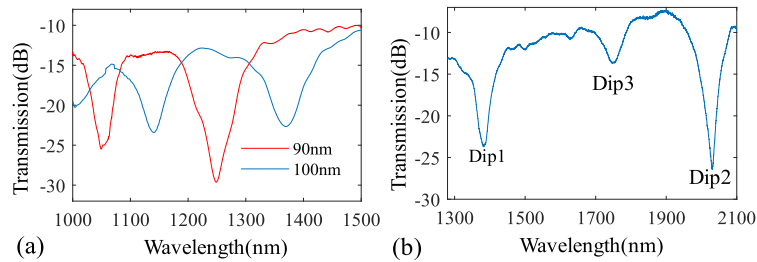

Fig. 5. (a) Transmission spectra of samples coated to different SnO_2 film thicknesses. (b) Transmission spectrum of a sample coated with a 100 nm thickness SnO_2 film, observing in the range 1300 - 2100 nm.
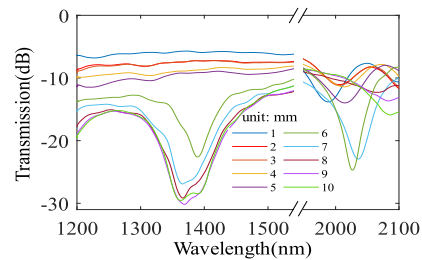
Fig. 6. Transmission spectra of a sample coated with 100 nm thickness SnO_2 film, for different depths of immersion into water.

To evaluate the sensitivity to RI changes of the optical fiber sensor designed, samples were immersed in glycerol solutions having a RI in the range from 1.336-1.363, where the spectral drift was monitored with the RI value changing in steps of 0.003. Repeated experiments were carried out (this was done 3 times), and the repeatability of RI response seen as a result was good. Figure 7(a) illustrates the spectra for these different values of RI. As the RI increases, both the LMR dip and coupling dip exhibit a red shift. The clear linear relationship was observed between the dip wavelength and the RI, as illustrated in Fig. 7(b). Within the RI range of 1.336-1.363, the average sensitivity of the LMR dip reached 3812.5 nm/RIU, while the average sensitivity of the coupling dip was 1310.3 nm/RIU.

The temperature characteristics of the sensor were evaluated. The sensor was immersed into deionized water and then placed into a temperature and humidity-controlled chamber, set to a constant humidity of 90%. The temperature was increased from 25 to 70 °C in steps of 5 °C, and the measurement was repeated 3 times. The center wavelengths of the resonance dips were seen to change with temperature, and so the temperature sensitivities of Dip 1 and Dip 2 at RI values of 1.336 and 1.339 were obtained and are displayed in Fig. 8. The temperature average sensitivity of the LMR dip was -521.4 pm/°C, while that of the directional coupling dip was found to be -286.6 pm/°C for the RI of 1.336. As the RI of the liquid used increases to 1.339,
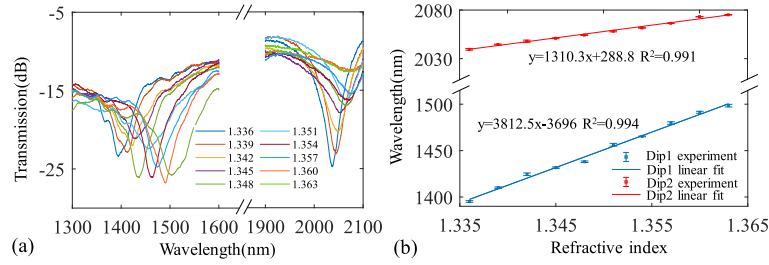
Fig. 7. (a) Transmission spectra for solution with the RI in range of 1.336-1.363. (b) RI sensitivities of Dip 1 and Dip 2.

the resonant wavelength shifts to the longer wavelength side, while the temperature sensitivities remain almost constant during the experiment.
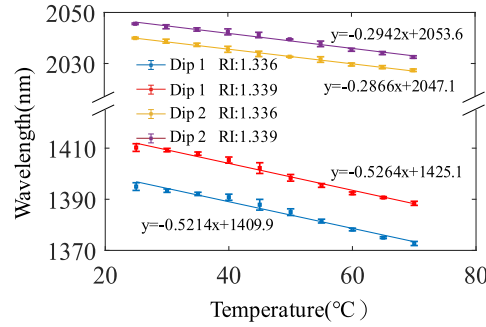
Fig. 8. Temperature sensitivities of Dip 1 and Dip 2 at RI values of 1.336 and 1.339.

Based on the different responses of the Dip 1 and Dip 2 to changes in both the RI and temperature, the following matrix equation was constructed and can be used to determine the RI and temperature simultaneously:

$$\begin{pmatrix} \Delta\lambda_1 \\ \Delta\lambda_2 \end{pmatrix} = \begin{pmatrix} K_{n1} & K_{T1} \\ K_{n2} & K_{T2} \end{pmatrix} \begin{pmatrix} \Delta n \\ \Delta T \end{pmatrix} \tag{2}$$

where $\Delta\lambda_1$ and $\Delta\lambda_2$ are the wavelength shifts of Dip 1 and Dip 2, and Δn and ΔT are the changes of RI and temperature. K_{n1} and K_{n2} are the RI sensitivity coefficients of Dip 1 and Dip 2, respectively, while K_{T1} and K_{T2} are the temperature sensitivity coefficients of Dip 1 and Dip 2, respectively. According to the experimental results obtained, $K_{n1} = 3812.5$ nm/RIU, $K_{n2} = 1310.3$ nm/RIU, $K_{T1} = -521.4$ nm/°C, $K_{T2} = -286.6$ nm/°C. Thus Eq. (2) can be expressed as:

$$\begin{pmatrix} \Delta\lambda_1 \\ \Delta\lambda_2 \end{pmatrix} = \begin{pmatrix} 3812.5\text{nm/RIU} & -521.4\text{pm/°C} \\ 1310.3\text{nm/RIU} & -286.6\text{pm/°C} \end{pmatrix} \begin{pmatrix} \Delta n \\ \Delta T \end{pmatrix} \tag{3}$$

There are some inevitable errors in the measurement results owing to the effect of external disturbances, such as system errors and minor fluctuations in the physical quantities to be measured. The high performance in the presence of such interference factors is a key factor for the sensor, particularly in the case of two-parameter sensing [28]. $\Delta\lambda_{i1}$ and $\Delta\lambda_{i2}$ are the wavelength shifts of Dip 1 and Dip 2 caused by these external interference effects, respectively.

Thus Eq. (3) can be expressed as:

$$\begin{pmatrix} \Delta\lambda_1 + \Delta\lambda_{i1} \\ \Delta\lambda_2 + \Delta\lambda_{i2} \end{pmatrix} = \begin{pmatrix} K_{n1} & K_{T1} \\ K_{n2} & K_{T2} \end{pmatrix} \begin{pmatrix} \Delta n \\ \Delta T \end{pmatrix} \tag{4}$$

The RI error Δn_{error}, and the temperature error ΔT_{error}, resulting from the external interference effects can be expressed as:

$$\begin{pmatrix} \Delta n_{\text{error}} \\ \Delta T_{\text{error}} \end{pmatrix} = \frac{1}{|K|} \begin{pmatrix} K_{T2} & -K_{T1} \\ -K_{n2} & K_{n1} \end{pmatrix} \begin{pmatrix} \Delta n \\ \Delta T \end{pmatrix} \tag{5}$$

where $|K|$ can further be expressed as:

$$|K| = K_{T2}K_{n1} - K_{T1}K_{n2} \tag{6}$$

The smaller of the maximum values of Δn_{error} ($\Delta n_{\text{error, max}}$) and ΔT_{error} ($\Delta T_{\text{error, max}}$), the stronger will be the ability of sensor to operate well in the presence of interference effects. The external interference ranges here were recorded as a_n and a_T. The ratio of $\Delta n_{\text{error, max}}$ to the maximum value of a_n and the ratio of $\Delta T_{\text{error, max}}$ to the maximum value of a_T were used to evaluate Δn_{error} and ΔT_{error}. Thus, a_n and a_T could be expressed as:

$$\begin{cases} a_n = \left|\frac{K_{T1}}{|K|}\right| + \left|\frac{K_{T2}}{|K|}\right| \\ a_T = \left|\frac{K_{n1}}{|K|}\right| + \left|\frac{K_{n2}}{|K|}\right| \end{cases} \tag{7}$$

Smaller values of a_n and a_T result in smaller corresponding values of $\Delta n_{\text{error, max}}$ and $\Delta T_{\text{error, max}}$ respectively, thereby leading to greater ability of the sensor to work well in the presence of interference. The calculated values of a_n and a_T of the sensor developed were 1.97×10^{-6} °C/pm and 0.0125 RIU/pm, respectively.

The experiments reported above have demonstrated clearly that the sensor can measure both temperature and RI simultaneously. To illustrate this, the sample was placed in the temperature and humidity chamber where the 'reference' RI and temperature values were set to 1.336 and 25 °C, respectively. The temperature and RI were changed at the same time and set to the following sets of values (1.336, 30 °C), (1.336, 70 °C), (1.339, 60 °C) respectively. The value of $\Delta\lambda_1$ and $\Delta\lambda_2$ recorded were the wavelength shifts of Dip 1 and Dip 2. The corresponding values of RI (Δn_{mea}) and temperature (ΔT_{mea}) were obtained by use of Eq. (3), and the results obtained are shown in Table 1. It can be seen that the maximum measurement errors for the values of RI and temperature were 0.00095 and 0.9 °C respectively.

Table 1. Simultaneous detection of RI and temperature

Δn_{set}	ΔT_{set}(°C)	$\Delta\lambda_1$(nm)	$\Delta\lambda_2$(nm)	Δn_{mea}	ΔT_{mea}(°C)
0	5	-1.67	-1.2	0.00037	5.9
0	45	-22.33	-12.6	0.00042	45.9
0.003	35	-2.69	-4.58	0.00395	34.1

Table 2 shows the comparison of several different dual parameter sensors reported and the sensor designed here. The sensor reported in this work shows higher sensitivity in the measurement of the RI value [29–32,22] and temperature [29–30,22,24], compared to a number of sensors reported in the literature [22,24,29–32]. The sensor designed in this work can be sued simultaneously to measure both RI and temperature, (with good resistance to external interference effects) and which thus shows great potential in improving the accuracy of the measurement of these parameters, especially for biomedical applications.

Table 2. Comparison of performance of several reported RI and temperature dual-parameter sensors [literature reference] with the sensor designed in this work

Structure	RI sensitivity (nm/RIU)	Temperature sensitivity (pm/°C)	Ref.
MZI	1354; 43	10.2; 20.6	[29]
FPI + FBG	-1210.49; 0	-189; -11	[30]
U shaped interferometer	−777.95; −1705.66	106; 134	[24]
SPR	1546; -248	0; -830	[31]
PCF + LPFG	117.28; 92.14	9.14; -86.29	[22]
SPR	2323.4; 0	-2850; -280	[32]
LMR + directional coupler	3812.5; 1310.3	-521.4; -286.6	**This work**

4. Conclusions

In summary, this work has shown the design and performance of a dual-parameter sensor based on side-polished HADCF. The HADCF was welded between two SMFs, and the exposed suspended core was coated with SnO_2 film to excite the LMR, this being combined with the directional coupling of the two cores to realize the two-parameter measurement, in a sensor of length 10 mm. The operating mechanisms of LMR and directional coupler were used, and integrated into a single piece of HADCF in parallel to allow both RI and temperature to be simultaneously measured, and the sensor is highly integrated. The RI and the temperature sensitivities of the LMR dip observed were 3812.5 nm/RIU and -521.4 nm/°C. Further, the RI and temperature sensitivities of the directional coupling dip were measured to be 1310.3 nm/RIU and -286.6 nm/°C, respectively. The sensor reported in this work has the advantages of simplicity in manufacture, high sensitivity, a strong immunity to interference effects, a high level of integration, small size and capability for two-parameter measurement, with important potential in improving measurement accuracy in biomedicine as a result.

Disclosures. The authors declare no conflicts of interest.

Data availability. Data underlying the results presented in this paper are not publicly available at this time but may be obtained from the authors upon reasonable request.

References

1. D. Gao, C. Guan, Y. Wen, *et al.*, "Multi-hole fiber based surface plasmon resonance sensor operated at near-infrared wavelengths," Opt. Commun. **313**, 94–98 (2014).
2. D. S. Rivero, A. B. Socorro-Lcránoz, and I. D. Villar, "Direct functionalization of TiO_2/PSS sensing layer for an LMR-based optical fiber reusable biosensor," IEEE Sensors J. **23**(24), 30437–30443 (2023).
3. Z. Yin, X. Jing, K. Li, *et al.*, "Experimental study of an intensity-modulated curvature sensor with high sensitivity based on microstructured optical fiber," Opt. Express **31**(3), 4770 (2023).
4. Z. Yin and X. Jing, "Visible-NIR surface plasmon resonance sensing technology for high precision refractive index detection," Opt. Lett. **49**(6), 1477–1480 (2024).
5. O. Fuentes, P. Vaiano, I. del Villar, *et al.*, "Improving the width of lossy mode resonances in a reflection configuration D-shaped fiber by nanocoating laser ablation," Opt. Lett. **45**(17), 4738–4741 (2020).
6. D. P. Sudas, V. A. Jitov, G. G. Yakushcheva, *et al.*, "Increasing the sensitivity of chemically resistant lossy mode resonance-based sensors on Al_2O_3 coatings," Opt. Mater. (Amsterdam, Neth.) **149**, 115031 (2024).
7. P. Saccomandi, "Design considerations of an ITO-coated U-shaped fiber optic LMR biosensor for the detection of antibiotic ciprofloxacin," Biosensors **13**(3), 362 (2023).
8. W. M. Zhao, Q. Wang, X. Z. Wang, *et al.*, "Theoretical and experimental research of lossy mode resonance-based high-sensitivity optical fiber refractive index sensors," J. Opt. Soc. Am. B **36**(8), 2069–2078 (2019).
9. N. Paliwal, N. Punjabi, J. John, *et al.*, "Design and fabrication of lossy mode resonance based U-shaped fiber optic refractometer utilizing dual sensing phenomenon," J. Lightwave Technol. **34**(17), 4187–4194 (2016).

10. A. Vicente, D. Santano, P. Zubiate, *et al.*, "Lossy mode resonance sensors based on nanocoated multimode-coreless-multimode fibre," Sens. Actuators, B **304**, 126955 (2020).

11. S. Choudhary, F. Esposito, L. Sansone, *et al.*, "Lossy mode resonance sensors in uncoated optical fiber," IEEE Sensors J. **23**(14), 15607–15613 (2023).

12. X. Z. Wang and Q. Wang, "Theoretical analysis of a novel microstructure fiber sensor based on lossy mode resonance," Electronics (Basel, Switz.) **8**(5), 484 (2019).

13. Z. Li, X. Yang, F. Wang, *et al.*, "Discriminating bulk and surface refractive index changes with fiber-tip leaky mode resonance," J. Lightwave Technol. **41**(13), 4341–4351 (2023).

14. I. D. Villar, C. R. Zamarreno, M. Hernaez, *et al.*, "Lossy mode resonance generation with indium-tin-oxide-coated optical fibers for sensing applications," J. Lightwave Technol. **28**(1), 111–117 (2010).

15. Q. Wang, X. Li, W. M. Zhao, *et al.*, "Lossy mode resonance-based fiber optic sensor using layer-by-layer SnO_2 thin film and SnO_2 nanoparticles," Appl. Surf. Sci. **492**, 374–381 (2019).

16. C. L. Tien, T. C. Mao, and C. Y. Li, "Lossy Mode Resonance sensors fabricated by RF magnetron sputtering GZO thin film and D-shaped fibers," Coatings **10**(1), 29 (2020).

17. J. D. Lopez, I. R. Matias, R. C. D. S. Allil, *et al.*, "Ultrahigh refractive index sensitivity with lossy mode resonance in a side-polished low-index polymer optical fiber," IEEE Trans. Instrum. Meas. **73**, 1–9 (2024).

18. F. J. Arregui, I. D. Villar, C. R. Zamarreño, *et al.*, "Giant sensitivity of optical fiber sensors by means of lossy mode resonance," Sens. Actuators, B **232**, 660–665 (2016).

19. A. Ozcariz, M. Dominik, M. Smietana, *et al.*, "Lossy mode resonance optical sensors based on indium-gallium-zinc oxide thin film," Sens. Actuators, A **290**, 20–27 (2019).

20. K. Vikas, R. K. Walia, and Verma, "Lossy mode resonance-based uniform core tapered fiber optic sensor for sensitivity enhancement," Commun. Theor. Phys. **72**(9), 095502 (2020).

21. Y. Liu, C. Wei, Z. Shen, *et al.*, "Multi-tapered polarization-maintaining fiber-optic sensor for refractive index and temperature measurements," Opt. Fiber Technol. **81**, 103569 (2023).

22. C. Du, Q. Wang, S. Hu, *et al.*, "Simultaneous measurement of refractive index and temperature based on a long period fiber grating inscribed in a photonic crystal fiber with an electric-arc discharge," Instrum. Sci. Technol. **47**(2), 185–194 (2019).

23. F. Zhu, X. Hao, Y. Zhang, *et al.*, "D-shaped optic fiber temperature and refractive index sensor assisted by tilted fiber Bragg grating and PDMS film," Sens. Actuators, A **346**, 113870 (2022).

24. J. Ge, Y. Zhang, W. Zhang, *et al.*, "Simultaneous Measurement of RI and Temperature Based on Compact U-Shaped Interferometer," IEEE Sensors J. **20**(7), 3593–3598 (2020).

25. J. Yang, C. Guan, P. Tian, *et al.*, "In-fiber refractive index sensor based on single eccentric hole-assisted dual-core fiber," Opt. Lett. **42**(21), 4470–4473 (2017).

26. M. Marciniak, J. Grzegorzewski, and M. Szustakowski, "Analysis of lossy mode cut-off conditions in planar waveguides with semicon-ductor guiding layer," IEE Proc.-J **140**(4), 247–252 (1993).

27. X. Chen, M. Li, J. Koh, *et al.*, "Effects of bending on the performance of hole-assisted single polarization fibers," Opt. Express **15**(17), 10629–10636 (2007).

28. X. Li, C. Wang, Z. Wang, *et al.*, "Anti-external interference sensor based on cascaded photonic crystal nanobeam cavities for simultaneous detection of refractive index and temperature," J. Lightwave Technol. **37**(10), 2209–2216 (2019).

29. A. D. Gomes and O. Frazão, "Microfiber knot with taper interferometer for temperature and refractive index discrimination," IEEE Photonics Technol. Lett. **29**(18), 1 (2017).

30. Y. G. Liu, X. Liu, T. Zhang, *et al.*, "Integrated FPI-FBG composite all-fiber sensor for simultaneous measurement of liquid refractive index and temperature," Opt. Lasers Eng. **111**, 167–171 (2018).

31. C. Teng, P. Shao, R. Min, *et al.*, "Simultaneous measurement of refractive index and temperature based on a side-polish and V-groove plastic optical fiber SPR sensor," Opt. Lett. **48**(2), 235–238 (2023).

32. J. S. Velázquez-González, D. Monzón-Hernández, D. Moreno-Hernández, *et al.*, "Simultaneous measurement of refractive index and temperature using a SPR-based fiber optic sensor," Sens. Actuators, B **242**, 912–920 (2017).